1482 Vol. 35, No. 7 / July 2018 / Journal of the Optical Society of America B Research Article

Journal of the Optical Society of America B
OPTICAL PHYSICS

Line-current model for deriving the wavelength scaling of linear and nonlinear optical properties of thin elongated metallic rod antennas

M. L. Nesterov,[1] M. Schäferling,[1] K. Weber,[1] F. Neubrech,[1,2] H. Giessen,[1] and T. Weiss[1,*]

[1]4th Physics Institute and Research Center SCoPE, University of Stuttgart, Pfaffenwaldring 57, D-70550 Stuttgart, Germany
[2]Kirchhoff-Institute for Physics, University of Heidelberg, Im Neuheimer Feld 227, D-69120 Heidelberg, Germany
*Corresponding author: t.weiss@pi4.uni-stuttgart.de

Received 16 January 2018; revised 27 February 2018; accepted 16 April 2018; posted 19 April 2018 (Doc. ID 319861); published 4 June 2018

Thin elongated rod antennas with a diameter smaller than the skin depth exhibit surface plasmon polariton modes that can propagate along the antenna while being reflected at the antenna ends. In the line-current model, a current is associated with these modes in order to approximate the optical properties of the antennas. We find that it is crucial to correctly derive the reflection of the surface plasmon polariton modes at the antenna ends for predicting the resonance position and shape accurately. Thus, the line-current model allows for deriving the wavelength scaling behavior of plasmonic near fields as well as the emitted third-harmonic intensity efficiently. Neglecting the frequency dependence of the nonlinear susceptibility, we find that the third-harmonic intensity of such metallic rod antennas scales as the fourth power of the frequency, whereas it decreases with the twelfth power within the limit of the generalized Miller's rule. © 2018 Optical Society of America

OCIS codes: (250.5403) Plasmonics; (240.6680) Surface plasmons; (190.2620) Harmonic generation and mixing.

https://doi.org/10.1364/JOSAB.35.001482

1. INTRODUCTION

Plasmonic resonances in metallic antennas concentrate electromagnetic fields in small volumes and, thus, amplify and control light–matter interaction. This includes the spontaneous emission rate and the directivity of quantum emitters [1–6], the enhancement of circular dichroism signals [7–10] and Faraday rotation [11–13], second- and third-harmonic generation [14–18], advanced concepts for optical refractive index sensors [19–24], and antenna-assisted surface-enhanced infrared absorption spectroscopy [23,25,26].

As shown in [27], plasmonic resonances in wire antennas can be understood in analogy to Fabry–Perot modes by considering the wire antenna as a cavity for surface plasmon polaritons propagating along the wire. At the wire ends, the surface plasmon polariton is partially reflected, propagates in the opposite direction, and is reflected at the other end. Resonances occur for constructive interference of the surface plasmon polariton after one round trip. The difference to classical antennas is that the wavelength of the surface plasmon polariton significantly differs from the free-space wavelength and the field can penetrate into the antenna for the plasmon modes, as we require working in a regime in which the diameter is smaller than the skin depth of the metal. Based on these considerations, Dorfmüller *et al.* have developed a line-current model for predicting the near field of the plasmonic resonances in the vicinity of thin elongated wire antennas for illumination by far-field incidence [28]. The approach has then been adapted to near-field excitation by quantum emitters in [29], where also the influence of the radiation damping due to the reflection at the antenna ends is taken into account by a simple approximation. More sophisticated models for the reflection at the antenna ends rely on analytical calculations restricted to flat antenna ends [30] as well as numerical simulations for more complex geometries [31,32].

In this paper, we combine the line-current model for far-field incidence [28] with the near-field formulation described in [29]. Furthermore, we replace the approximate consideration of the radiation damping in [29] by numerical simulations of the reflection of a surface plasmon polariton at the antenna end. Comparison with full numerical simulation of the three-dimensional rod antenna geometries reveals that this approach provides a significantly better estimation of the antenna properties compared with the aforementioned approaches.

Our numerical simulations of the surface plasmon polariton and its reflection at the antenna end as well as the reference simulations of the optical properties of the entire antenna geometry are carried out using the finite element method. While the numerical simulation of an entire three-dimensional antenna geometry can be rather time- and memory-consuming, the simulations of the surface plasmon polariton and its reflection at the antenna end can be carried out very efficiently, as they are effectively two-dimensional. Most importantly, these two-dimensional simulations are independent of the antenna length, so that the results of the line-current model can be given as an analytical function of the antenna length. Thus, it is possible to derive the wavelength scaling behavior of the optical response of thin elongated wire antennas in a fast and efficient manner.

We demonstrate here how to use the line-current model for predicting the wavelength scaling of the electromagnetic near fields, which is highly relevant for resonantly enhanced refractive index sensing [22,24] as well as antenna-assisted surface-enhanced infrared absorption spectroscopy [23]. Furthermore, we derive the wavelength scaling of the resonantly enhanced third-harmonic signal from thin wire antennas.

2. LINE-CURRENT MODEL

The fundamental idea of the line-current model is sketched in Fig. 1. An incident field excites a current in the antenna. The current propagates to the antenna end, where it is partially reflected and partially transmitted. In the limit of a thin wire, the current predominantly stems from the fundamental surface plasmon polariton mode, i.e., a mode that propagates along the long wire axis and is bound in the other directions. The forward and backward propagating surface plasmon polariton results in an oscillating current distribution, from which we can calculate the radiation to the far field.

The material surrounding the antenna is modeled via its dielectric permittivity ε_1; the permittivity of the metallic antenna is ε_2. In our examples, we are using $\varepsilon_1 = 1$ and ε_2 defined by experimental permittivity data of gold [33]. The corresponding wavenumbers are $k_1 = \sqrt{\varepsilon_1}k_0$ and $k_2 = \sqrt{\varepsilon_2}k_0$, respectively, with $k_0 = \omega/c$. The long axis of the antenna is oriented along the z direction, and the antenna length is denoted by L_0. The cross section normal to the z direction has a circular shape with radius R; the antenna ends are semispheres. When we consider properties of the full antenna, such as scattering and absorption cross section, we will henceforth use spherical coordinates ρ, ϑ, and φ with unit vectors $\hat{\rho}$, $\hat{\vartheta}$, and $\hat{\varphi}$. The origin of the coordinate system is located at the center of the antenna. The incident angle is defined as $\theta = \pi/2 - \vartheta^{\mathrm{inc}}$. For the current propagating along the antenna in the z direction, we will consider a cylindrical coordinate system with coordinates ρ, ϕ, and z, with unit vectors $\hat{\rho}$, $\hat{\phi}$, and $\hat{z}$.

The electric field of the fundamental surface plasmon polariton propagating along an infinitely long metal cylinder (radius R) has a vanishing ϕ component. It is given in the exterior region ($\rho > R$) by

$$E_\rho^{(1)} = -iE_1 \frac{k_\mathrm{p}}{\kappa_1} H_1^{(1)}(\kappa_1\rho)\mathrm{e}^{ik_\mathrm{p}z}, \qquad E_z^{(1)} = E_1 H_0^{(1)}(\kappa_1\rho)\mathrm{e}^{ik_\mathrm{p}z}, \tag{1}$$

where $H_l^{(1)}$ denotes Hankel functions of first kind and order l. The time dependence $\exp(-i\omega t)$ has been omitted for the sake of simplicity. Furthermore, $\kappa_1^2 = k_1^2 - k_\mathrm{p}^2$. In the interior region ($\rho \le R$), we obtain

$$E_\rho^{(2)} = -iE_2 \frac{k_\mathrm{p}}{\kappa_2} J_1(\kappa_2\rho)\mathrm{e}^{ik_\mathrm{p}z}, \qquad E_z^{(2)} = E_2 J_0(\kappa_2\rho)\mathrm{e}^{ik_\mathrm{p}z}. \tag{2}$$

Here, J_l denotes Bessel functions of the first kind and order l, and $\kappa_2^2 = k_2^2 - k_\mathrm{p}^2$. The propagation constant k_p can be determined from the following transcendental equation [27]:

$$\frac{\varepsilon_2(\omega)}{\kappa_2 R}\frac{J_1(\kappa_2 R)}{J_0(\kappa_2 R)} - \frac{\varepsilon_1}{\kappa_1 R}\frac{H_1^{(1)}(\kappa_1 R)}{H_0^{(1)}(\kappa_1 R)} = 0. \tag{3}$$

Figure 2 depicts the calculated dispersion relation of the fundamental surface plasmon polariton mode propagating in an infinitely long gold cylinder of radius $R = 10$ nm in vacuum.

A. Derivation of Current and Far-Field Properties

The incident field $\mathbf{E}^{\mathrm{inc}}$ induces a current $\mathbf{j}$ inside the rod antenna that results in a scattered field $\mathbf{E}^{\mathrm{scat}}$ outside the antenna. The total field in the exterior is given by $\mathbf{E}^{\mathrm{tot}} = \mathbf{E}^{\mathrm{inc}} + \mathbf{E}^{\mathrm{scat}}$ and is related to the internal field $\mathbf{E}^{\mathrm{int}}$ inside the antenna by the boundary conditions for Maxwell's equations. The induced current obeys

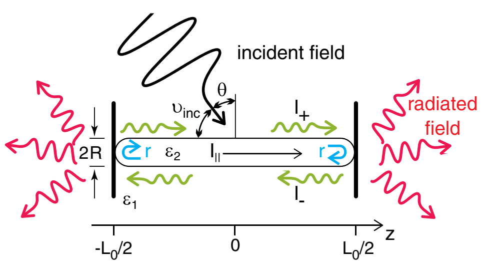

Fig. 1. Schematic of the line-current model for a rod antenna (permittivity ε_2) in homogeneous space (permittivity ε_1) with length L_0 and a cylindrical cross section of radius R. The incident field excites a surface plasmon polariton in the rod antenna, which propagates to the antenna ends, where it is partially reflected (reflection coefficient r). The forward (backward) propagating surface plasmon polariton is denoted by the current I_+ (I_-), and the driving current is $I_\parallel$. In this model, the field radiated by the antenna originates from the emission of the line current to the far field.

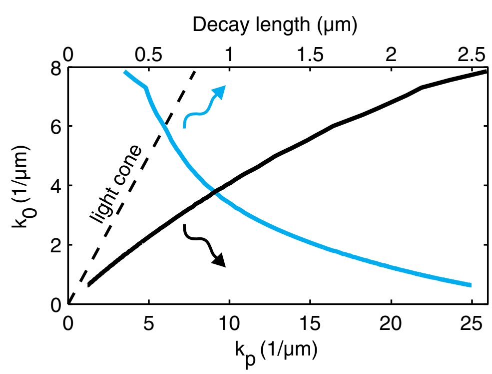

Fig. 2. Calculated dispersion relation (solid black line) for a surface plasmon polariton mode propagating in an infinitely long gold cylinder of radius $R = 10$ nm in vacuum. The blue solid curve denotes the corresponding decay length. The black dashed line is the light cone of vacuum.

$$\mathbf{j} = -i\omega\varepsilon_0 \underbrace{[\varepsilon_2(\omega) - \varepsilon_1]}_{\equiv\Delta\varepsilon} \mathbf{E}^{\mathrm{int}}. \tag{4}$$

For wire antennas thinner than the skin depth of the metal, we may assume that the current is approximately constant across the plane perpendicular to the wire. Furthermore, the electromagnetic field of the fundamental surface plasmon polariton propagating in such a thin wire does not depend on the azimuthal angle ϕ. It exhibits a dominant z component and a negligible ρ component, which follows from evaluating Eq. (2) for small arguments. Hence, the current $\mathbf{j}$ is predominantly z directed, with

$$\mathbf{j}(\mathbf{r}) \approx I(z)\Theta(R-\rho)\hat{z}. \tag{5}$$

Here, Θ denotes the Heaviside function. For the current $I(z)$, we might make the following ansatz [28] in order to account for the contributions of the incident field as well as the surface plasmon polariton propagating with k_{p} along the wire:

$$I(z) = I_{\parallel} e^{ik_{\parallel}z} + I_{+} e^{ik_{\mathrm{p}}z} + I_{-} e^{-ik_{\mathrm{p}}z}. \tag{6}$$

In this case, $k_{\parallel} \equiv k_1 \sin\theta$ denotes the component of the incident wave vector parallel to the wire antenna.

Let us now relate the different contributions in Eq. (6) to the incident field. The vector potential associated with the current in Eq. (6) is [34]

$$\mathbf{A}(\mathbf{r}) = \frac{\mu_0}{4\pi}\int dV' \mathbf{j}(\mathbf{r}') \frac{e^{ik_1|\mathbf{r}-\mathbf{r}'|}}{|\mathbf{r}-\mathbf{r}'|}. \tag{7}$$

Using Eq. (5) in Eq. (7) as well as $|\mathbf{r}-\mathbf{r}'| \approx \sqrt{\rho^2 + (z-z')^2}$, we obtain

$$\mathbf{A}(\mathbf{r}) \approx \frac{\mu_0}{4\pi} S_R \hat{z} \int_{-L_0/2}^{L_0/2} dz' I(z') \frac{e^{ik_1\sqrt{\rho^2+(z-z')^2}}}{\sqrt{\rho^2+(z-z')^2}}. \tag{8}$$

If we assume that $\rho \ll \lambda_1$ with $\lambda_1 = 2\pi/k_1$, the second factor in the integrand in Eq. (8) becomes localized around z. Hence, we may change variables from z' to $\zeta + z$ and extract $I(\zeta = 0) = I(z)$ from the integral, resulting in

$$\mathbf{A}(\mathbf{r}) \approx \frac{\mu_0}{4\pi} S_R \hat{z} I(z) \underbrace{\int_{z-L_0/2}^{z+L_0/2} d\zeta \frac{e^{ik_1\sqrt{\rho^2+\zeta^2}}}{\sqrt{\rho^2+\zeta^2}}}_{\equiv\tilde{Z}}, \tag{9}$$

with $S_R = 2\pi R^2$ being the area of the rod cross section. According to [28], $\tilde{Z}$ takes the role of a characteristic impedance.

The z component of the scattered field at the wire surface can be calculated from Eq. (9) as

$$E_z^{\mathrm{scat}}(z,R) = \frac{i\omega}{k_1^2}(k_1^2 + \partial_z^2)A_z = \frac{i\omega}{k_1^2}\frac{\mu_0}{4\pi} S_R \tilde{Z}(k_1^2 + \partial_z^2) I(z). \tag{10}$$

The boundary condition for the z component of the electric fields at the surface of the metal wire is

$$E_z^{\mathrm{scat}}(z,R) + E_z^{\mathrm{inc}}(z,R) = E_z^{\mathrm{int}}(z,R). \tag{11}$$

The incident field can be assumed constant across the wire, i.e., $E_z^{\mathrm{inc}} = E_0^{\mathrm{inc}} \cos\theta \exp(ik_{\parallel}z)$. Together with Eqs. (4) and (5) as well as Eq. (10), this results in

$$E_0^{\mathrm{inc}} \cos\theta e^{ik_{\parallel}z} + \frac{i\omega}{k_1^2}\frac{\mu_0}{4\pi} S_R \tilde{Z}(k_1^2 + \partial_z^2) I(z) = \frac{iI(z)}{\omega\varepsilon_0\Delta\varepsilon}. \tag{12}$$

Using Eq. (6) and the fact that the resulting equations have to be fulfilled independently for all values of $k_{\parallel}$ and k_{p}, we obtain according to [28] that

$$I_{\parallel} = -i\omega\varepsilon_0\Delta\varepsilon\Delta k E_0^{\mathrm{inc}} \cos\theta, \tag{13}$$

with

$$\Delta k \equiv \frac{k_1^2 - k_{\mathrm{p}}^2}{k_{\parallel}^2 - k_{\mathrm{p}}^2}. \tag{14}$$

Furthermore, we assume in our model that only the current with amplitude $I_{\pm}$ is transmitted at $z = \pm L/2$, so that the current reflected at the antenna ends obeys

$$z = L_0/2: \quad I_{-} e^{-ik_{\mathrm{p}}L/2} = -I_{\parallel} e^{ik_{\parallel}L/2} - rI_{+} e^{ik_{\mathrm{p}}L/2}, \tag{15}$$

$$z = -L_0/2: \quad I_{+} e^{-ik_{\mathrm{p}}L/2} = -I_{\parallel} e^{-ik_{\parallel}L/2} - rI_{-} e^{ik_{\mathrm{p}}L/2}. \tag{16}$$

Here, r denotes the reflection of the surface plasmon polariton at the antenna ends and is in general a complex number. However, following [29], we can redefine r to be real by introducing an effective antenna length $L = L_0 + \Delta L$. The relation between reflection phase ϕ_{r} and antenna length increase ΔL is then given by $\Delta L = \phi_{\mathrm{r}}/k_{\mathrm{p}}$. *It has to be emphasized that the line-current model with effective antenna length is not fully equivalent to the one with complex reflection coefficient*. This is due to the imaginary part of k_{p}, which results in additional artificial absorption when replacing the real antenna length by the effective length. In the following, we will consider real r and effective antenna length L, as it provides a better agreement with the numerically exact results. The reason might be that the line-current model does not properly account for radiative losses at the antenna ends, which is counterbalanced by the overestimation of the Ohmic losses when using the effective antenna length.

Equations (15) and (16) straightforwardly result in

$$I_{\pm} = I_{\parallel} \frac{re^{ik_{\mathrm{p}}^{\pm}L/2} - e^{-ik_{\mathrm{p}}^{\pm}L/2}}{1 - r^2 e^{2ik_pL}} e^{ik_{\mathrm{p}}L}, \tag{17}$$

with $k_{\mathrm{p}}^{\pm} \equiv k_{\mathrm{p}} \pm k_{\parallel}$. Note that k_{p} as well as L and r are functions of frequency ω. The roots of the denominator at frequencies ω_m provide the resonance condition for the wire antenna in the same way as in a standard Fabry–Perot cavity [27,35]: the real part of ω_m is the resonance frequency, while $-2\,\mathrm{Im}(\omega_m)$ defines the linewidth of the resonance.

In summary, the current $I(z)$ inside the rod antenna is given by

$$I(z;\omega;k_{\parallel}) = -i\omega\varepsilon_0\Delta\varepsilon(\omega)\Delta k(\omega;k_{\parallel})\hat{I}(z;\omega;k_{\parallel})E_0^{\mathrm{inc}} \cos\theta. \tag{18}$$

For brevity of notations, we have introduced here the normalized current:

$$\hat{I}(z;\omega;k_{\parallel}) = e^{ik_{\parallel}z} + \hat{I}_{+}(z;\omega;k_{\parallel}) + \hat{I}_{-}(z;\omega;k_{\parallel}), \tag{19}$$

with $\hat{I}_{\pm} = \exp(\pm ik_{\mathrm{p}}z)I_{\pm}/I_{\parallel}$.

In the far-field limit, the scattered field is polarized transverse to the outgoing wave vector, which means that the only relevant component for our resonance geometry is the ϑ component, for which we obtain [29]

$$
\begin{aligned}
E_\vartheta(\rho,\vartheta) &\approx iZ_1k_1S_R\frac{e^{ik_1\rho}}{4\pi\rho}\sin\vartheta\int_{-L/2}^{L/2}dzI(z)e^{-ik_1\cos\vartheta z}\\
&= k_0^2\Delta\varepsilon\Delta k\frac{e^{ik_1\rho}}{4\pi\rho}\sin\vartheta V_A\left\{\operatorname{sinc}\left[(k_\parallel-k_1\cos\vartheta)\frac{L}{2}\right]\right.\\
&\quad+\hat{I}_+(0)\operatorname{sinc}\left[(k_p-k_1\cos\vartheta)\frac{L}{2}\right]\\
&\quad\left.+\hat{I}_-(0)\operatorname{sinc}\left[(k_p+k_1\cos\vartheta)\frac{L}{2}\right]\right\}E_0^{\mathrm{inc}}\cos\theta. \qquad \textbf{(20)}
\end{aligned}
$$

Here, we have introduced $V_A = LS_R$ as the effective volume of the antenna, $\operatorname{sinc}(x) = \sin(x)/x$, and Z_1 denotes the impedance in medium 1. According to Eqs. (4)–(6) as well as Eq. (18), the z component of the electric field inside the antenna is

$$E_z^{\mathrm{int}}(z) \approx \Delta k\hat{I}(z)E_0^{\mathrm{inc}}\cos\theta. \qquad \textbf{(21)}$$

Based on Eqs. (20) and (21), we can calculate the extinction, scattering, and absorption cross sections as

$$\sigma_{\mathrm{ext}} = \sigma_{\mathrm{scat}} + \sigma_{\mathrm{abs}}, \qquad \textbf{(22)}$$

$$\sigma_{\mathrm{scat}} = \frac{P_{\mathrm{rad}}}{S_0} = \frac{2\pi\rho^2}{|E_0^{\mathrm{inc}}|^2}\int_0^\pi d\vartheta|E_\vartheta|^2\sin\vartheta, \qquad \textbf{(23)}$$

$$\sigma_{\mathrm{abs}} = \frac{P_{\mathrm{abs}}}{S_0} \approx \frac{k_1\operatorname{Im}(\varepsilon_2)}{\varepsilon_1|E_0^{\mathrm{inc}}|^2}\frac{V_A}{L}\int_{-L/2}^{L/2}dz|E_z^{\mathrm{int}}|^2, \qquad \textbf{(24)}$$

where $S_0 = |E_0^{\mathrm{inc}}|^2/2Z_1$ is the time-averaged Poynting vector amplitude of the incident plane wave. The integrals in Eqs. (23) and (24) can be carried out numerically. Note that Eq. (20) implies that the scattering cross section σ_{scat} is proportional to $k_0^4V_A^2$, whereas Eqs. (5) and (6) result in $\sigma_{\mathrm{abs}} \propto k_0V_A$, as in the case of small spherical antennas, because

$$
\begin{aligned}
&\frac{1}{L}\int_{L/2}^{L/2}dz|E_z^{\mathrm{int}}|^2\\
&\propto \frac{1}{L}\int_{L/2}^{L/2}dz|\hat{I}(z)|^2 = 1 + |\hat{I}_+(0)|^2 + |\hat{I}_-(0)|^2\\
&\quad+2\operatorname{Re}\left[\hat{I}_+(0)\operatorname{sinc}\left(k_p^-\frac{L}{2}\right)+\hat{I}_-(0)\operatorname{sinc}\left(k_p^+\frac{L}{2}\right)\right]\\
&\quad+2\operatorname{Re}[\hat{I}_+(0)\hat{I}_-^*(0)]\operatorname{sinc}[\operatorname{Re}(k_p)L]. \qquad \textbf{(25)}
\end{aligned}
$$

B. Discussion

In the above derivations, we have made the following approximations:

- **Thin-wire approximation:** Equation (5) is based on the assumption that the wire antenna has a radius smaller than the skin depth of the metal, so that we can assume a current inside the antenna that does not depend on ρ. Furthermore, the thin-wire approximation allows for the assumption that the incident field is constant in the plane normal to the long wire axis. However, the exact spatial dependence of the fields might have some impact on the excitation efficiency, because the z component of the electric field at the antenna surface might be smaller or larger than in the center of the antenna. This also affects the accuracy of the estimated near-field distribution around the antenna.
- **Single-mode approximation:** Only the fundamental surface plasmon polariton is considered as a possible mode propagating along the thin wire. Higher-order surface plasmon polaritons with field nodes in the radial or azimuthal direction as well as leaky modes are neglected. These modes provide additional radiative and nonradiative loss channels that are not taken into account in the line-current model. Similarly, the incident field not only excites currents in the form of Eq. (6), but should contain the excitation of the other modes as well. Consequently, the single-mode approximation results in an incorrect estimation of the current amplitudes $I_\pm$ and $I_\parallel$. However, for elongated thin wires, the single-mode approximation is justified, because the fundamental surface plasmon polariton is in this case the only bound mode with a considerably large decay length compared to the antenna length. For short antennas, however, higher-order modes become more relevant [32,36].
- **Disregard of excitation and radiation at antenna ends:** The main excitation of the surface plasmon polariton is assumed to stem from the incident electric field at the surface of the elongated rod antenna. Similarly, the radiation to the far field is assumed to take place through the current oscillating in the whole antenna. The accumulated charges at the antenna ends as well as the possibility to excite the surface plasmon polariton from these ends are neglected. This approximation as well as all other approximations in the line-current model fail for larger diameters, for which it will result in an inaccurate estimation of the charge amplitude $I(z)$ and its radiation to the far field.

In addition, we have not yet specified the reflection amplitude r and the effective antenna length $L = L_0 + \Delta L$. In the work of Dorfmüller *et al.* [28], the magnitude of the reflection coefficient is assumed to equal unity ($r = 1$), while ΔL is obtained from fitting the line-current model to full numerical results.

It has to be emphasized that $r = 1$ means neglecting the radiative decay, i.e., the radiation damping. This is of course a very rough approximation, since the oscillating current does radiate to the far field. In [29], it is therefore suggested to first calculate the so-called radiation resistance R_{rad} for $r = 1$, with

$$R_{\mathrm{rad}} = \frac{2P}{I_{\max}^2}, \qquad \textbf{(26)}$$

where P is the total emitted power and $I_{\max}$ is the maximum of $|I(z)|$. This value can be used in order to derive a better estimation for the reflection coefficient:

$$r(L_0) \approx \frac{\operatorname{Re}(Z) - R_{\mathrm{rad}}/2}{\operatorname{Re}(Z) + R_{\mathrm{rad}}/2} \equiv r_{\mathrm{app}}. \qquad \textbf{(27)}$$

In this case, Z denotes the antenna wave impedance calculated from the surface plasmon polariton mode in the infinitely long wire as

$$Z = \frac{\int dxdyE_xH_y^* - E_yH_x^*}{|\int dxdyI(z)|^2}. \qquad \textbf{(28)}$$

For the effective antenna length increase, a simple approximation is given by $\Delta L_{\mathrm{app}} = 2R$ [27]. Alternatively, we have calculated the reflection coefficient r and the effective antenna length increase ΔL of the fundamental surface plasmon polariton mode at the rod antenna end using full numerical simulations based on the finite element method (see Fig. 3). For that purpose, we have set up a model, in which we launch the surface plasmon polariton at a port at the antenna end. Perfectly matched layers ensure the appropriate boundary conditions for the scattered light, and the reflection into the surface plasmon polariton mode is derived in a second port. The resulting reflection amplitude and effective antenna length increase are denoted by r_{FEM} and ΔL_{FEM}, respectively.

Figure 4 depicts the scattering cross section of gold rod antennas with a diameter of $R = 10$ nm, where the antenna length is varied between 150 nm and 500 nm. The thin black line has been calculated using the finite element method for the full antenna, while the thick lines have been derived from the various approximations in the line-current model. In panel (a), we have used $r = 1$ in combination with the approximate effective antenna length increase ΔL_{app} (magenta lines) as well as the value ΔL_{FEM} (green lines) extracted from the two-dimensional finite element simulation of the reflection at the antenna end. Panel (b) depicts the results calculated from the approximate reflection amplitude r_{app} with the approximate effective antenna length increase ΔL_{app} (orange lines) as well as results that are solely based on the finite element simulation of the reflection at the antenna end (blue lines).

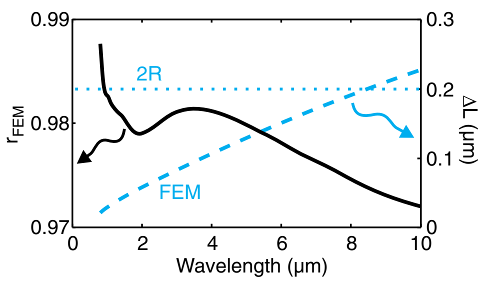

Fig. 3. Magnitude of the reflection coefficient r_{FEM} (black solid line) and effective antenna length increase ΔL_{FEM} (blue dashed line) for the reflection of a surface plasmon polariton mode at a rounded antenna end with antenna radius $R = 10$ nm calculated by the finite element method (FEM). The blue dotted line denotes the simple approximation $\Delta L_{\mathrm{app}} = 2R$ of Ref. [27].

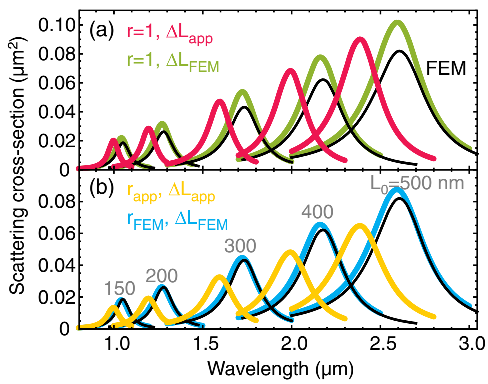

Fig. 4. Scattering cross section for antenna length between 150 mm and 500 nm and a radius of 10 nm. Thin black lines denote full numerical simulations based on the finite element method (FEM), whereas thick lines are derived from the line-current model using different approximations: (a) approximate effective antenna length increase ΔL_{app} (magenta lines) and numerically calculated effective antenna length increase ΔL_{FEM} (green lines) at the antenna ends without radiation damping ($r = 1$); (b) approximate effective antenna length increase ΔL_{app} and radiation damping based on the reflection magnitude r_{app} (orange lines) as well as numerically calculated effective antenna length increase ΔL_{FEM} and radiation damping based on r_{FEM} (blue lines).

It can be seen in Fig. 4(a) that the simple approximation of $r = 1$ overestimates the magnitude of the scattering cross section. Furthermore, using ΔL_{app}, the resonance wavelength of the line-current model (magenta lines) is shifted compared to the result of the full numerical simulation. The shift of the resonance wavelength originates in the simple approximation for the effective antenna length. The mismatch in resonance wavelength almost vanishes when using ΔL_{FEM} (green lines). In order to obtain a better agreement between the magnitude of the scattering cross section from the line-current model and the full numerical simulations, one has to replace $r = 1$ by r_{app} from Eq. (27) or r_{FEM} from the finite element simulation for the reflection at the antenna end. When combining r_{app} with ΔL_{app} [orange lines in Fig. 4(b)], the magnitude of the scattering cross section is reduced compared to Fig. 4(a), while the resonance wavelength is shifted. This mismatch in resonance wavelength vanishes when combining r_{app} with ΔL_{FEM} (not shown here). However, taking the maxima of the scattering cross sections as a guide to the eye, one can see that r_{app} underestimates the magnitude of the scattering cross section. In contrast, the numerically derived magnitude r_{FEM} of the reflection coefficient and the resulting effective antenna length L_{FEM} yield an excellent agreement between the line-current model and full numerical simulations, as seen for the blue lines in Fig. 4(b).

Note that the dimensions of our elongated rod antennas with a radius of $R = 10$ nm are in a regime where the thin-wire approximation and the single-mode approximation can be applied. For radii larger than the skin depth, the agreement between the line-current model and full numerical simulations becomes worse, so that the line-current model can be used only for qualitative predictions, as shown in [23].

3. APPLICATIONS

A. Wavelength Scaling

Whenever it is desired to predict the wavelength scaling behavior of antenna properties such as maximum scattering cross section or enhancement of the near fields, numerical simulations rely on solving Maxwell's equations repeatedly. Hence, full-field simulations become rather inefficient, while the line-current model provides the required results in significantly less calculation time. As an example, we derive here the wavelength scaling of the magnitude of the electric field in the vicinity of the wire antenna at the fundamental resonance, which is important for sensing applications, such as antenna-assisted surface-enhanced infrared absorption spectroscopy [23,25].

Near resonances, $|\hat{I}_{\pm}| \gg 1$, so that Eq. (19) can be written as

$$\hat{I}(z;\omega;k_\parallel) \approx \hat{I}_+(z;\omega;k_\parallel) + \hat{I}_-(z;\omega;k_\parallel) \equiv \hat{I}_\mathrm{p}(\zeta;\omega;k_\parallel), \tag{29}$$

which is a function of $\zeta \equiv k_\mathrm{p} z$. This functional behavior in the z direction due to the dominating surface plasmon polariton is valid even beyond the limits of the line-current model when being close to a resonance. Therefore, we may approximate the electric field inside the layer including the weak radial dependence as

$$E_z^\mathrm{int}(\rho,z) \approx E_0^\mathrm{int} J_0(\kappa_2\rho) f(k_\mathrm{p} z), \tag{30}$$

$$E_\rho^\mathrm{int}(\rho,z) = \frac{1}{\kappa_2^2}\frac{\partial E_z^\mathrm{int}}{\partial\rho\partial z} = -E_0^\mathrm{int}\frac{k_\mathrm{p}}{\kappa_2} J_1(\kappa_2\rho)\frac{\partial f}{\partial\zeta}, \tag{31}$$

where f specifies the z dependence of the fields. For small values of ρ, the z component is roughly constant while the ρ component is much smaller for $k_\mathrm{p}\rho \ll 1$, thus revealing the basic assumption of the line-current model:

$$E_z^\mathrm{int}(\rho,z) \approx E_0^\mathrm{int} f(k_\mathrm{p} z), \tag{32}$$

$$E_\rho^\mathrm{int}(\rho,z) \approx -E_0^\mathrm{int}\frac{k_\mathrm{p}\rho}{2}\frac{\partial f}{\partial\zeta}. \tag{33}$$

Using Eqs. (21) and (29) in Eq. (33) in combination with the boundary condition for the radial field component, the ρ component in the exterior yields

$$E_\rho^\mathrm{ext}(\rho,z) \approx \frac{\varepsilon_2}{\varepsilon_1}\frac{k_\mathrm{p} R}{2}\frac{\partial I_\mathrm{p}}{\partial\zeta}\frac{H_1^{(1)}(\kappa_1\rho)}{H_1^{(1)}(\kappa_1 R)}\Delta k E_0^\mathrm{inc}\cos\theta. \tag{34}$$

The z component in the exterior is approximately given by

$$E_z^\mathrm{ext}(\rho,z) \approx -\hat{I}_\mathrm{p}(\zeta;\omega;k_\parallel)\frac{H_0^{(1)}(\kappa_1\rho)}{H_0^{(1)}(\kappa_1 R)}\Delta k E_0^\mathrm{inc}\cos\theta. \tag{35}$$

It turns out that $|\partial\hat{I}_\mathrm{p}/\partial\zeta| \gg |2\varepsilon_1\hat{I}_\mathrm{p}/k_\mathrm{p}R\varepsilon_2|$, so that the dominant field component in the exterior is the ρ component.

As mentioned above, the strength of the near field is important for antenna-assisted surface-enhanced infrared absorption spectroscopy. In this case, a thin layer of molecules is placed directly on the antenna surface. If the layer is thinner than the decay length of the surface plasmon polariton outside the antenna, the ρ component in Eq. (34) is roughly constant in the radial direction. Defining V_m as the volume of the molecules, we thus obtain for the normalized near-field intensity in the volume of the molecules

$$\int_{V_\mathrm{m}} \mathrm{d}V\left|\frac{E_\rho(\rho,z)}{E_0^\mathrm{inc}\cos\theta}\right|^2 = \frac{|\varepsilon_2 k_\mathrm{p} R|^2}{4\varepsilon_1^2}|\Delta k|^2 S_R\int_{-L/2}^{L/2}\mathrm{d}z\left|\frac{\partial\hat{I}_\mathrm{p}}{\partial\zeta}\right|^2. \tag{36}$$

In Fig. 5, we are displaying the result of Eq. (36) at the resonance wavelength for varying antenna lengths and a fixed radius of 10 nm (blue line). The prediction of the line-current model agrees well with finite element results of the corresponding antenna geometries (orange dots). For such thin rod antennas, the overall scaling follows a $\lambda^{1.2}$ scaling (thin black dashed line), while there is a λ^3 scaling for thicker antennas (for details, see [23]) with a radius of 100 nm that is well above the skin depth of our metal (25–27 nm in the wavelength range of interest). Interestingly, the line-current model allows for predicting the λ^3 scaling for thicker antennas, but it can no longer predict the magnitude of the field enhancement (not shown here).

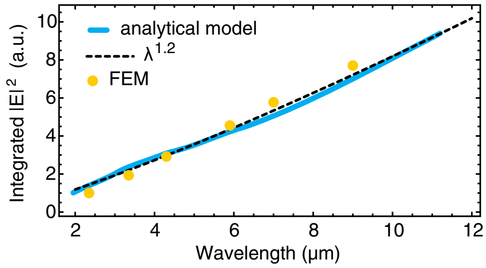

Fig. 5. Wavelength scaling of the near-field intensity around an elongated rod antenna with a radius of 10 nm. The blue curve has been obtained from the line-current model by evaluating Eq. (36) at the resonance wavelength for varying antenna lengths. The results are in good agreement with the numerical results derived by finite element modeling of the corresponding antenna geometries (orange dots). The thin black dashed line depicts a $\lambda^{1.2}$ scaling as a guide to the eye.

B. Third-Harmonic Generation

The full numerical simulation of third-harmonic generation is rather time-consuming, even in the undepleted pump approximation [37], where any back-action of the field at the third harmonic to the fundamental wavelength is neglected. The reason is that the wavelength at the third harmonic is one third of the incident wavelength, requiring a very fine mesh to resolve all features in the electromagnetic near fields. In the line-current model, all numerical simulations are effectively two-dimensional, thus reducing the numerical effort significantly. The third-harmonic intensity can be calculated using the reciprocity principle [38]. In a first step, the electric fields are calculated at the fundamental wavelength, i.e., at frequency ω. This provides the nonlinear polarization $\mathbf{P}_\mathrm{TH}$ at the third harmonic 3ω, which acts as a source for the emitted electric field $\mathbf{E}_\mathrm{TH}$ at the third harmonic. Given another source $\mathbf{j}'$ that generates a field $\mathbf{E}'$, the reciprocity theorem states

$$\int \mathrm{d}V\mathbf{j}'\cdot\mathbf{E}_\mathrm{TH} = -i3\omega\int\mathrm{d}V\mathbf{P}_\mathrm{TH}\cdot\mathbf{E}'. \tag{37}$$

Assuming $\mathbf{j}' = \hat{\mathbf{j}}\delta(\mathbf{r}-\mathbf{r}')$ with $|\hat{\mathbf{j}}| = 1$ and $\mathbf{r}'$ being located in the homogenous surrounding of the wire antenna, the analytic solution for the Green's dyadic in homogeneous space results in

$$\begin{aligned}\mathbf{E}'_\mathrm{ext}(\mathbf{r}) &= ik_1 Z_1\left[\hat{\mathbf{j}}\left(1+\frac{ik_1|\mathbf{R}|-1}{k_1^2|\mathbf{R}|^2}\right)\right.\\ &\quad\left.+\mathbf{R}(\mathbf{R}\cdot\hat{\mathbf{j}})\frac{3-3ik_1|\mathbf{R}|-k_1^2|\mathbf{R}|^2}{k_1^2|\mathbf{R}|^4}\right]\frac{\mathrm{e}^{ik_1|\mathbf{R}|}}{4\pi|\mathbf{R}|}\\ &\approx ik_1 Z_1\hat{\mathbf{j}}\frac{\mathrm{e}^{ik_1 r'}}{4\pi r'}\mathrm{e}^{-ik_1\cos\vartheta' z} \equiv ik_1 Z_1\hat{\mathbf{j}}\frac{\mathrm{e}^{ik_1 r'}}{4\pi r'}\mathrm{e}^{-ik'_\parallel z},\end{aligned} \tag{38}$$

where $\mathbf{R} = \mathbf{r}-\mathbf{r}'$, and we have used the thin-wire approximation as well as $r' \gg r$. The field in Eq. (38) acts as an incident field at frequency 3ω, which can be put into the line-current model in order to derive the internal field occurring in Eq. (37).

In particular, we have to replace $E_0^{\text{inc}} \cos\theta$ in Eq. (21) by $\mathbf{E}'_{\text{ext}} \cdot \hat{z} \exp(ik'_{\|}z)$, which provides for $\hat{\mathbf{j}} \perp \mathbf{r}'$ the transverse field components emitted at the third harmonic:

$$\begin{aligned}\hat{\mathbf{j}} \cdot \mathbf{E}_{\text{TH}}(\mathbf{r}') \approx{}& (3k_0)^2 \frac{e^{ik_1(3\omega)r'/c}}{4\pi r'} \chi^{(3)} \\ &\times [\Delta k(\omega) E_0^{\text{inc}} \cos\theta]^3 \Delta k(3\omega) \sin\vartheta' \\ &\times \frac{V_A}{L} \int_{-L/2}^{L/2} \mathrm{d}z [\hat{I}(z;\omega;k_{\|})]^3 \hat{I}(z;3\omega;-k'_{\|}). \end{aligned} \quad (39)$$

The integral in Eq. (39) can be easily evaluated. The third-harmonic intensity emitted in a certain direction and polarization is then proportional to $|\hat{\mathbf{j}} \cdot \mathbf{E}_{\text{TH}}|^2$.

Since Eq. (17) enters in $\hat{I}(z;\omega;k_{\|})$ and $\hat{I}(z;3\omega;-k'_{\|})$, we deduce that the third-harmonic intensity becomes significantly increased due to a resonance at the fundamental harmonic, as $\hat{I}(z;\omega;k_{\|})$ contributes with the third power in Eq. (39). A resonance at the third harmonic increases the third-harmonic intensity as well, but it only enters with first power in $\hat{I}(z;3\omega;-k'_{\|})$. These findings are confirmed in Fig. 6, where we calculated the third-harmonic intensity emitted in the x direction and z polarization using Eq. (39) for different antenna lengths (blue lines). Black arrows indicate one third of the resonance wavelength of the fundamental resonance at ω_1, whereas red arrows depict the position of the third-order resonance at ω_3. For longer antennas, these resonances become more and more matched, i.e., $3\omega_1 \approx \omega_3$.

Neglecting the frequency dependence of $\chi^{(3)}$, the overall scaling of the third-harmonic intensity follows a λ^{-4} behavior, as shown by the orange line in Fig. 6. The reason is that the integral in Eq. (39) is roughly constant over frequency. Thus, the only frequency scaling of the field comes from the prefactor ω^2, so that the third-harmonic intensity scales with $\omega^4 \propto \lambda^{-4}$.

In its range of applicability, the generalized Miller's rule [39] provides

$$\chi^{(3)}(3\omega) \propto \chi^{(1)}(3\omega)[\chi^{(1)}(\omega)]^3. \quad (40)$$

For a Drude metal with $\chi^{(1)}(\omega) \propto \omega^{-2}$, we thus obtain that $\chi^{(3)}(3\omega) \propto \omega^{-8}$. The third-harmonic intensity of the gold rod antenna is proportional to ω^4 times the square value of $\chi^{(3)}$, so that it scales as $\omega^{-12} \propto \lambda^{12}$. Hence, the third-harmonic intensity grows with antenna length, until Miller's rule breaks down.

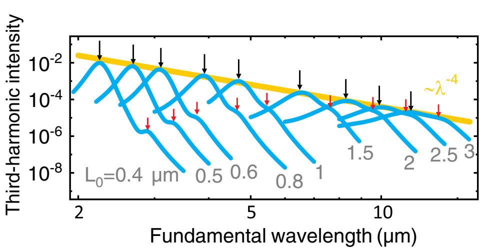

Fig. 6. z-polarized third-harmonic intensity (blue lines) emitted in the x direction by rod antennas of 10 nm radius and varying lengths between 400 nm and 3 μm. The results have been obtained from the line-current model and the reciprocity theorem for $\chi^{(3)} = 1$. The thick orange line is a guide to the eye for the asymptotic scaling of the maximum intensity. Black arrows indicate one third of the fundamental resonance wavelength, whereas red arrows denote the resonance wavelength of the third-order resonance.

4. SUMMARY

We have shown that, within the single-mode approximation, the line-current model is capable of predicting the optical properties of thin elongated metal antennas. This requires, however, to accurately know the reflection coefficient of the propagating surface plasmon mode at the antenna ends. Simple models for the reflection coefficient fail, while we can calculate it efficiently by numerical approaches, such as the finite element method. It has to be emphasized that the resulting numerical effort is significantly lower than that required to simulate the optical properties of the full three-dimensional antenna, because the required numerical calculations for the line-current model are effectively two-dimensional. Most importantly, the line-current model allows for covering a large range of antenna length with negligible computational effort, which can be used for predicting the wavelength scaling behavior of certain resonant properties, such as the near-field enhancement as well as the third-harmonic intensity. For the latter, we obtain a λ^{-4} scaling from the line-current model when neglecting the frequency dependence of $\chi^{(3)}$. Combining this result with the generalized Miller's rule, we obtain an overall λ^{12} scaling of the third-harmonic intensity.

Funding. Bundesministerium für Bildung und Forschung (BMBF) (13N9048, 13N10146); H2020 European Research Council (ERC) (COMPLEXPLAS); Baden-Württemberg Stiftung (Internationale Spitzenforschung II); Ministerium für Wissenschaft, Forschung und Kunst Baden-Württemberg (MWK) (Zukunftsoffensive IV); Volkswagen Foundation; Deutsche Forschungsgemeinschaft (DFG) (SPP1839); Alexander von Humboldt Foundation.

REFERENCES

1. E. M. Purcell, "Spontaneous emission probabilities at radio frequencies," Phys. Rev. **69**, 681 (1946).
2. C. Sauvan, J. P. Hugonin, I. S. Maksymov, and P. Lalanne, "Theory of the spontaneous optical emission of nanosize photonic and plasmon resonators," Phys. Rev. Lett. **110**, 237401 (2013).
3. G. M. Akselrod, C. Argyropoulos, T. B. Hoang, C. Ciracì, C. Fang, J. Huang, D. R. Smith, and M. H. Mikkelsen, "Probing the mechanisms of large Purcell enhancement in plasmonic nanoantennas," Nat. Photonics **8**, 835–840 (2014).
4. E. A. Muljarov and W. Langbein, "Exact mode volume and Purcell factor of open optical systems," Phys. Rev. B **94**, 235438 (2016).
5. A. G. Curto, G. Volpe, T. H. Taminiau, M. P. Kreuzer, R. Quidant, and N. F. van Hulst, "Unidirectional emission of a quantum dot coupled to a nanoantenna," Science **329**, 930–933 (2010).
6. D. Dregely, K. Lindfors, M. Lippitz, N. Engheta, M. Totzeck, and H. Giessen, "Imaging and steering an optical wireless nanoantenna link," Nat. Commun. **5**, 4354 (2014).
7. A. O. Govorov, Z. Fan, P. Hernandez, J. M. Slocik, and R. R. Naik, "Theory of circular dichroism of nanomaterials comprising chiral molecules and nanocrystals: plasmon enhancement, dipole interactions, and dielectric effects," Nano Lett. **10**, 1374–1382 (2010).
8. E. Hendry, T. Carpy, J. Johnston, M. Popland, R. V. Mikhaylovskiy, A. J. Lapthorn, S. M. Kelly, L. D. Barron, N. Gadegaard, and M. Kadodwala, "Ultrasensitive detection and characterization of biomolecules using superchiral fields," Nat. Nanotechnol. **5**, 783–787 (2010).
9. M. L. Nesterov, X. Yin, M. Schäferling, H. Giessen, and T. Weiss, "The role of plasmon-generated near fields for enhanced circular dichroism spectroscopy," ACS Photonics **3**, 578–583 (2016).

10. W. Zhang, T. Wu, R. Wang, and X. Zhang, “Surface-enhanced circular dichroism of oriented chiral molecules by plasmonic nanostructures,” J. Phys. Chem. C **121**, 666–675 (2016).
11. V. I. Belotelov, L. L. Doskolovich, and A. K. Zvezdin, “Extraordinary magneto-optical effects and transmission through metal-dielectric plasmonic systems,” Phys. Rev. Lett. **98**, 077401 (2007).
12. J. Y. Chin, T. Steinle, T. Wehlus, D. Dregely, T. Weiss, V. I. Belotelov, B. Stritzker, and H. Giessen, “Nonreciprocal plasmonics enables giant enhancement of thin-film faraday rotation,” Nat. Commun. **4**, 1599 (2013).
13. D. Floess, T. Weiss, S. G. Tikhodeev, and H. Giessen, “Lorentz nonreciprocal model for hybrid magnetoplasmonics,” Phys. Rev. Lett. **117**, 063901 (2016).
14. H. Aouani, M. Navarro-Cia, M. Rahmani, T. P. H. Sidiropoulos, M. Hong, R. F. Oulton, and S. A. Maier, “Multiresonant broadband optical antennas as efficient tunable nanosources of second harmonic light,” Nano Lett. **12**, 4997–5002 (2012).
15. K. Thyagarajan, S. Rivier, A. Lovera, and O. J. Martin, “Enhanced second-harmonic generation from double resonant plasmonic antennae,” Opt. Express **20**, 12860–12865 (2012).
16. H. Aouani, M. Rahmani, M. Navarro-Cia, and S. A. Maier, “Third-harmonic-upconversion enhancement from a single semiconductor nanoparticle coupled to a plasmonic antenna,” Nat. Nanotechnol. **9**, 290–294 (2014).
17. M. Hentschel, T. Utikal, H. Giessen, and M. Lippitz, “Quantitative modeling of the third harmonic emission spectrum of plasmonic nanoantennas,” Nano Lett. **12**, 3778–3782 (2012).
18. B. Metzger, M. Hentschel, T. Schumacher, M. Lippitz, X. Ye, C. B. Murray, B. Knabe, K. Buse, and H. Giessen, “Doubling the efficiency of third harmonic generation by positioning ITO nanocrystals into the hot-spot of plasmonic gap-antennas,” Nano Lett. **14**, 2867–2872 (2014).
19. A. B. Dahlin, J. O. Tegenfeldt, and F. Höök, “Improving the instrumental resolution of sensors based on localized surface plasmon resonance,” Anal. Chem. **78**, 4416–4423 (2006).
20. N. Liu, M. Mesch, T. Weiss, M. Hentschel, and H. Giessen, “Infrared perfect absorber and its application as plasmonic sensor,” Nano Lett. **10**, 2342–2348 (2010).
21. A. E. Cetin, A. F. Coskun, B. C. Galarreta, M. Huang, D. Herman, A. Ozcan, and H. Altug, “Handheld high-throughput plasmonic biosensor using computational on-chip imaging,” Light Sci. Appl. **3**, e122 (2014).
22. T. Weiss, M. Mesch, M. Schäferling, H. Giessen, W. Langbein, and E. A. Muljarov, “From dark to bright: first-order perturbation theory with analytical mode normalization for plasmonic nanoantenna arrays applied to refractive index sensing,” Phys. Rev. Lett. **116**, 237401 (2016).
23. K. Weber, M. L. Nesterov, T. Weiss, M. Scherer, M. Hentschel, J. Vogt, C. Huck, W. Li, M. Dressel, H. Giessen, and F. Neubrech, “Wavelength scaling in antenna-enhanced infrared spectroscopy: towards the far-IR and THz region,” ACS Photonics **4**, 45–51 (2017).
24. T. Weiss, M. Schäferling, H. Giessen, N. A. Gippius, S. G. Tikhodeev, W. Langbein, and E. A. Muljarov, “Analytical normalization of resonant states in photonic crystal slabs and periodic arrays of nanoantennas at oblique incidence,” Phys. Rev. B **96**, 045129 (2017).
25. F. Neubrech, A. Pucci, T. W. Cornelius, S. Karim, A. García-Etxarri, and J. Aizpurua, “Resonant plasmonic and vibrational coupling in a tailored nanoantenna for infrared detection,” Phys. Rev. Lett. **101**, 157403 (2008).
26. F. Neubrech, C. Huck, A. Pucci, and H. Giessen, “Surface-enhanced infrared spectroscopy using resonant nanoantennas,” Chem. Rev. **117**, 5110–5145 (2017).
27. L. Novotny, “Effective wavelength scaling for optical antennas,” Phys. Rev. Lett. **98**, 266802 (2007).
28. J. Dorfmüller, R. Vogelgesang, W. Khunsin, C. Rockstuhl, C. Etrich, and K. Kern, “Plasmonic nanowire antennas: experiment, simulation, and theory,” Nano Lett. **10**, 3596–3603 (2010).
29. T. H. Taminiau, F. D. Stefani, and N. F. van Hulst, “Optical nanorod antennas modeled as cavities for dipolar emitters: evolution of sub- and super-radiant modes,” Nano Lett. **11**, 1020–1024 (2011).
30. R. Gordon, “Reflection of cylindrical surface waves,” Opt. Express **17**, 18621–18629 (2009).
31. S. B. Hassan, R. Filter, A. Ahmed, R. Vogelgesang, R. Gordon, C. Rockstuhl, and F. Lederer, “Relating localized nanoparticle resonances to an associated antenna problem,” Phys. Rev. B **84**, 195405 (2011).
32. H. Jia, H. Liu, and Y. Zhong, “Role of surface plasmon polaritons and other waves in the radiation of resonant optical dipole antennas,” Sci. Rep. **5**, 8456 (2015).
33. M. A. Ordal, R. J. Bell, R. W. Alexander, L. L. Long, and M. R. Querry, “Optical properties of Au, Ni, and Pb at submillimeter wavelengths,” Appl. Opt. **26**, 744–752 (1987).
34. J. D. Jackson, *Classical Electrodynamics*, 3rd ed. (Wiley, 1999).
35. T. Weiss, N. A. Gippius, G. Granet, S. G. Tikhodeev, R. Taubert, L. Fu, H. Schweizer, and H. Giessen, “Strong resonant mode coupling of Fabry–Perot and grating resonances in stacked two-layer systems,” Photonics Nanostruct. Fundam. Appl. **9**, 390–397 (2011).
36. D. E. Chang, A. S. Sørensen, P. R. Hemmer, and M. D. Lukin, “Strong coupling of single emitters to surface plasmons,” Phys. Rev. B **76**, 035420 (2007).
37. T. Paul, C. Rockstuhl, and F. Lederer, “A numerical approach for analyzing higher harmonic generation in multilayer nanostructures,” J. Opt. Soc. Am. B **27**, 1118–1130 (2010).
38. K. O’Brien, H. Suchowski, J. Rho, A. Salandrino, B. Kante, X. Yin, and X. Zhang, “Predicting nonlinear properties of metamaterials from the linear response,” Nat. Mater. **14**, 379–383 (2015).
39. R. W. Boyd, *Nonlinear Optics*, 3rd ed. (Academic, 2008).

129.69.42.86 {ts '2018-08-29 01:29:26'}